EDGE ARTICLE

Check for updates

Holistic bulk-to-surface tailoring of Ni-rich cathodes for unlocking superior electrochemical stability

Yang Li,†[a] Zhixuan Liu,†[d] Haoji Wang,*[c] Jun Chen,*[cd] Zebo Gu,[b] Junyong Deng,[b] Guorong Liu,[b] Kun Huang,[b] Siyao Zhang,[b] Hao Feng,[b] Hao Chen,[b] Hongxin He,[a] Fuliang Zhu, [ID][e] Lina Hu,[b] Hongshuai Hou [ID] *[c] and Xiaobo Ji [ID] *[c]

Ni-rich cathodes have revolutionized lithium-ion batteries by delivering high energy density. However, achieving a durable trade-off between capacity and long life remains a formidable challenge, hindered by oxygen loss, irreversible phase transformation, and structural degradation during repeated cycles. Herein, we propose a synchronous bulk-to-surface full-scale modification strategy by integrating multi-site B/Ce bulk doping with a conformal CeO_2 surface coating. Boron atoms are successfully incorporated into transition metal (TM) tetrahedral interstitial sites as a covalent "rivet" to suppress detrimental H2–H3 phase transitions and anisotropic strain, thereby effectively inhibiting the intra-particle crack propagation. Concurrently, cerium ions are located at TM octahedral sites, acting as an electron buffer to decrease the concentration of reactive Ni^{4+} species and stabilize the oxygen lattice. Furthermore, the uniform CeO_2 protective layer serves as a robust physical barrier against electrolyte corrosion while effectively scavenging acidic species, reducing TM dissolution, and mitigating interfacial side reactions. The comprehensively regulated NCM83 cathode exhibits exceptional electrochemical performance, maintaining 94.4% capacity retention after 1000 cycles at 1C in a pouch-type full cell. This study presents an innovative approach that combines an internal multi-site lattice with an external surface structure for developing advanced Ni-rich cathodes.

1. Introduction

As key enablers of the worldwide shift toward sustainable energy and electrified mobility, lithium-ion batteries (LIBs) are considered as the dominant energy storage solution across multiple sectors, powering everything from consumer electronics to electric cars.[1–3] The operational characteristics of these batteries are fundamentally dictated by their components, in which cathode materials plays a decisive role in influencing critical parameters such as energy density, longevity, and charge–discharge stability.[4,5] Within the spectrum of available cathode options, Ni-rich layered $LiNi_xCo_yMn_{1−x−y}O_2$ compounds (where $x > 0.8$) have gained prominence for high-

performance LIBs applications due to their exceptional charge storage capability, favorable electrochemical potential, and robust cycling durability.[6–8] However, severe structural crisis is experienced upon extensive lithium extraction for Ni-rich layered cathodes.[9–11] Non-uniform lattice shrinkage associated with the H2–H3 phase change induces substantial mechanical strain both within crystalline domains and at particle interfaces.[12–14] The development of such stress precipitates the nucleation of internal microfractures and more severe inter-particle cleavage along mechanically weak boundaries.[15–17] These structural imperfections facilitate electrolyte penetration into newly exposed surfaces, thereby resulting in undesirable electrochemical reactions, metal ion leaching, and the formation of resistive surface films.[18–20] Of greater concern is the structural reorganization caused by transition metal (TM) cation migration in the crystalline planes, together with accumulated plastic deformation, leading to complete particle fragmentation.[21,22] This fragmentation in concert with the drastic catalytic properties of Ni^{4+} species amplifies electrolyte breakdown and surface film growth,[23–25] causing an irreversible conversion of the surface structure from an ordered layered arrangement to a disordered rock salt configuration similar to NiO.[26–29] The detrimental phase transition seriously degrades electrochemical performance by impeding charge transport and

[a]College of Materials Science and Engineering, Yangtze Normal University, Chongqing 408100, China

[b]CVC Testing Technology Co., Ltd, China National Electric Apparatus Research Institute Co., Ltd, Guangzhou 510000, China

[c]College of Chemistry and Chemical Engineering, Central South University, Changsha 410083, China

[d]Department of Chemistry/Department of Environment and Geography, University of York, York YO10 5DD, England, UK

[e]School of Metallurgy and Environment, Lanzhou University of Technology, Lanzhou 730050, China

† Y. Li and Z. Liu contributed equally to this work.

lithium ion mobility.[30–32] Furthermore, the heightened reactivity of surface Ni^{4+} and inherent oxygen instability collectively accelerate interface deterioration from layered to rock salt phase.[33,34]

To mitigate the capacity degradation of Ni-rich cathode materials, two fundamental challenges have to be concurrently address: bulk phase instability and interfacial side reactions.[35–37] Conventional modification approaches for Ni-rich cathodes primarily involve surface optimization and hetero-element doping.[38,39] Surface optimization is to create a physical protective barrier, typically through coatings of metal oxides, fluorides, or phosphates, to prevent direct electrolyte attack and HF corrosion.[40,41] For example, CeO_2 coatings have demonstrated efficacy in scavenging acidic species, suppressing transition metal dissolution, and mitigating interfacial side reactions.[42] Additionally, bulk doping contributes to enhancing the integrity of the lattice structure. Non-metallic elements like boron (B) can occupy interstitial sites to anchor the lattice, thereby restraining layer slip during phase transitions and improving mechanical stability.[43,44] Similarly, rare earth elements such as cerium (Ce), with their mixed valence states (Ce^{3+}/Ce^{4+}), function as electron buffers to reduce Ni^{4+} concentration and stabilize the oxygen framework.[45] Nevertheless, individual modification strategies typically target only one aspect of degradation. Surface coatings are largely ineffective in preventing bulk phase oxygen loss or phase transformation stress, while bulk doping generally fails to eliminate interfacial side reactions. Consequently, a synergistic approach is essential to simultaneously combat the multifaceted degradation mechanisms of Ni-rich cathodes from bulk to interface.

In this work, we develop a synchronous bulk-to-surface multifunctional regulation strategy to enhance both bulk and interfacial structural stability in $LiNi_{0.83}Co_{0.07}Mn_{0.1}O_2$ (NCM83) cathode materials. This approach combines B/Ce multi-site doping in the bulk phase with the construction of a uniform CeO_2 protective coating on particle surfaces. The tetrahedral interstitial B doping induces a "structural anchoring" effect, effectively mitigating anisotropic volume variations and suppressing microcrack formation. Concurrently, the TM octahedral Ce doping acts as an "electronic buffer" to stabilize the oxygen framework and minimize the generation of electrochemically active Ni^{4+} species. Furthermore, the conformal CeO_2 surface coating serves as a robust physical barrier against electrolyte corrosion while simultaneously scavenging acidic byproducts. Consequently, the NCM83-1.5BC pouch-type full cells demonstrate remarkable enhancements in electrochemical performance, maintaining 94.4% capacity retention after 1000 cycles at 1C. This work elucidates the synergistic stabilization mechanism achieved through the integration of bulk doping and surface modification, offering a novel design principle for developing next-generation Ni-rich cathode materials.

2. Results and discussion

The modification method was employed to modify the secondary particles of the NCM83 cathode through a one-step calcination process. B/Ce co-doping and CeO_2 coating were performed on the modified particles and the specific experimental details can be found in the Experimental section. ICP-OES elemental analysis reveals Ni, Co, Mn, B, and Ce, demonstrating excellent agreement with the designed stoichiometric ratios (Table S1). The pristine NCM83 cathode material exhibits spherical morphology (Fig. 1a) and the B/Ce-modified samples (NCM83-1.5BC) maintains similar morphological characteristics and particle size, effectively eliminating morphological influences on subsequent investigations (Fig. 1b). EDS analysis demonstrates a uniform distribution of B and Ce within the bulk of NCM83-1.5BC. In contrast, a slight enrichment of Ce at the particle surface is observed, providing clear evidence for the successful formation of a homogeneous CeO_2 surface coating (Fig. 1c). X-ray diffraction (XRD, Fig. 1d) and XAS were conducted to systematically investigate the crystalline structure of NCM83 and NCM83-1.5BC. Rietveld refinement (Fig. S1) confirms the layered structure of the cathode, with corresponding lattice parameters detailed in Table S2. Diffraction patterns indicate that all samples crystallize in the α-$NaFeO_2$ structure, with distinct peak splitting of (006)/(012) and (018)/(110) reflections confirming well-developed layered ordering. Notably, the (003) diffraction peak of B/Ce-modified samples exhibit a progressive shift toward lower 2θ values with increasing B/Ce content, demonstrating successful B/Ce incorporation into the crystal lattice and consequent expansion of (003) interplanar spacing. Rietveld refinement further reveals that B/Ce-co-doped induces a decrease in the a-axis parameter, while c-axis and unit cell volume (V) display opposing trends. The increase in the (003) interplanar spacing of NCM83-1.5BC primarily originates from the expansion of the inter-slab height LiO_6 (h_{Li-O}), which rises from 2.1137 Å (NCM83) to 2.1386 Å (NCM83-1.5BC). This expansion is conducive to the migration kinetics of lithium ions.

Density functional theory calculations of formation energies (Fig. 1e) indicate that B preferentially occupies tetrahedral interstitial sites and Ce preferentially occupies Ni octahedral sites, respectively. The co-doping of B and Ce affects the local electronic structure. Specifically, the presence of Ce ions, which can adopt a stable valence state, reduces the electron density on the surrounding oxygen anions. This electronic redistribution decreases the oxidative tendency of oxygen at high states of charge, leading to improved structural integrity of the oxygen layers. Furthermore, the B/Ce doping requires the partial reduction of Ni^{3+} to Ni^{2+} to achieve charge compensation. Ni K-edge analysis reveals an anomalous negative energy shift for NCM83-1.5BC (Fig. 1f), suggesting a reduced oxidation state of Ni in the bulk phase. Consistently, XPS results show an increased surface Ni^{2+} content in NCM83-1.5BC compared with NCM83 (Fig. S2). Furthermore, the CeO_2 coating layer effectively mitigates side reactions when the material is exposed to air, which is good agreement with the XPS results of C 1s and O 1s (Fig. S3). The analysis of the Ni K-edge FT-EXAFS and wavelet transform (Fig. 1g and i) indicates that the improved ordering of Ni–O bonds suggests that B/Ce modification likely stabilizes the oxygen lattice, reducing oxygen vacancies or local distortions, thereby rendering the NiO_6 octahedra more symmetric and
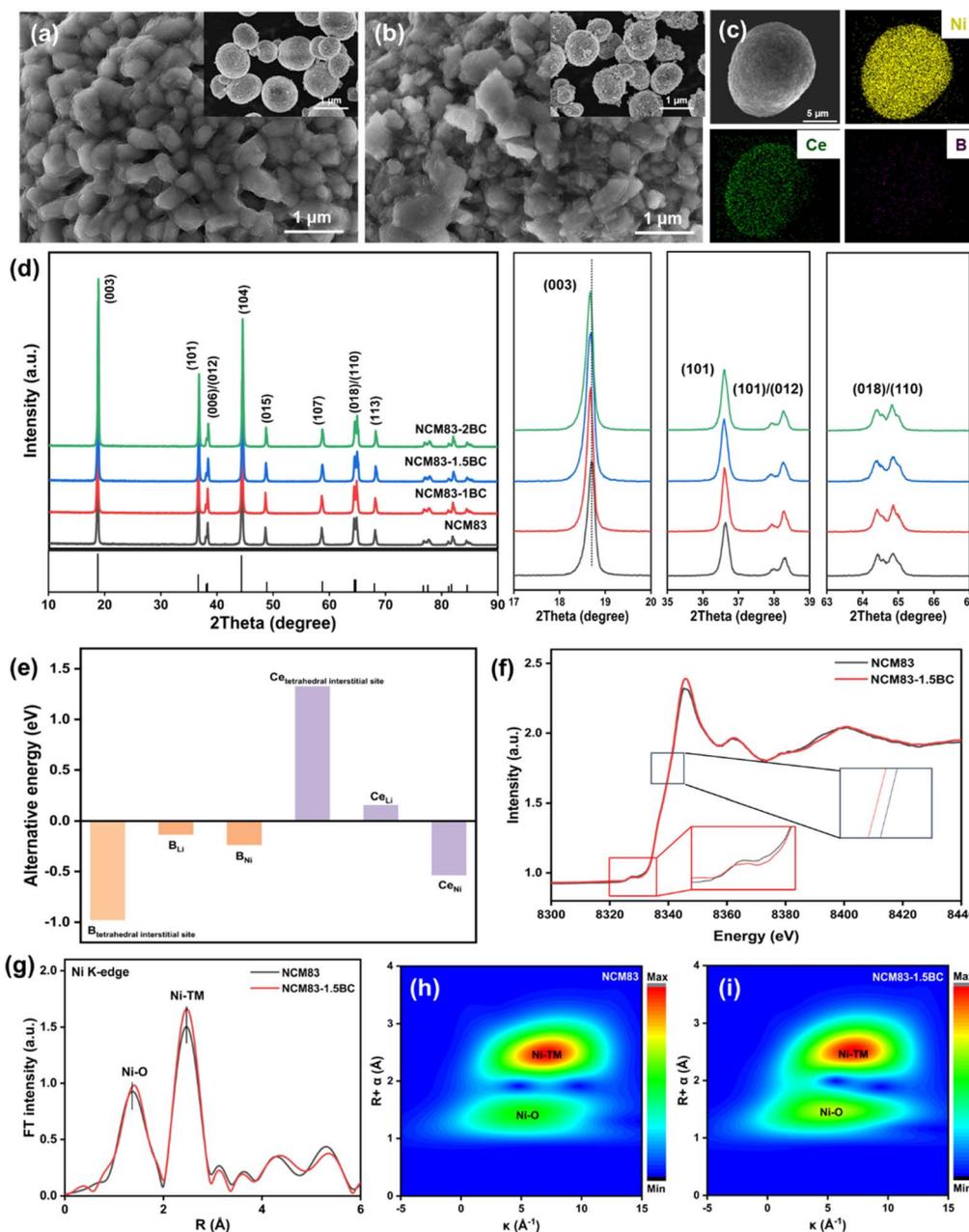
Fig. 1 (a and b) SEM images of NCM83 and NCM83-1.5BC cathode. (c) EDS mapping of Ni, Ce, and C for NCM83-1.5BC cathode. (d) XRD patterns of the NCM83 and B/Ce-modified NCM83 cathode with varied modification contents. (e) The formation energies of B and Ce substituted at different sites (tetrahedral interstitial, Li, and Ni). (f) The Ni K-edge XANES spectrum of the NCM83 and NCM83-1.5BC cathodes. (g) The FT-EXAFS and the fitting of the NCM83 and NCM83-1.5BC cathode. (h and i) Wavelet transform contour plots of EXAFS for the NCM83 and NCM83-1.5BC cathode.

stable. The significant enhancement in Ni–TM ordering directly reflects improved cation ordering within the transition metal layer, demonstrating that B/Ce modification effectively suppresses the migration of Ni^{2+} ions into the lithium layers during cycling and maintains the integrity of the layered structure. Collectively, the NCM83-1.5BC cathode exhibits optimized structural characteristics, including expanded LiO_2 intralayer spacing, strengthened Ni–O bonding, and consequently improved electrochemical performance.

Cross-sectional low-magnification high-angle annular dark-field-scanning transmission electron microscopy (HAADF-STEM) images reveal that NCM83 and NCM83-1.5BC exhibit similar morphological characteristics, suggesting that the B/Ce dual modification do not significantly alter their particle size distribution (Fig. 2a and d). The surface structure of the NCM83 particles exhibits a well-preserved layered configuration, without noticeable structural reconstruction layers or Li^+/Ni^{2+} mixing regions (Fig. 2b). Furthermore, the internal structure of
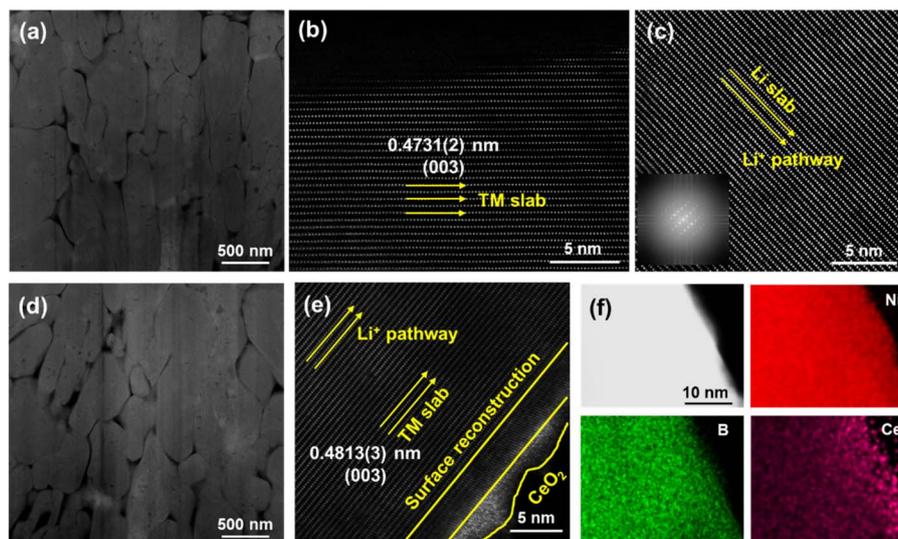
Fig. 2 (a and d) The cross-sectional low-magnification HAADF-STEM images of NCM83 and NCM83-1.5BC cathode. (b and c) The HAADF-STEM image from the surface and bulk region of the NCM83 cathode. (e) The HAADF-STEM image of the NCM83-1.5BC cathode. (f) STEM-EDS mapping for NCM83-1.5BC particle.

the NCM83 particles maintains a typical layered arrangement (Fig. 2c). Specifically, in the scanning transmission electron microscopy (STEM) images, intact transition metal (TM) layers present continuous white lattice fringes. HAADF-STEM characterization of NCM83-1.5BC confirms the preservation of the layered structure, with the sub-surface region enriched in B/Ce forming a distinct reconstruction layer beneath the CeO_2 coating (Fig. 2e). The NCM83-1.5BC sample exhibits a larger average interlayer spacing of the (003) crystallographic plane (0.4731(2) nm) than NCM83 (0.4813(3) nm), indicating that B/Ce doping increases the lattice parameter c. The outermost region of the NCM83-1.5BC particle exhibits distinct lattice fringes with an interplanar spacing of 0.163 nm in the HADDF-STEM image, which can be indexed to the (311) planes of the CeO_2 coating (Fig. S4). To confirm the presence of CeO_2 on the surface of NCM83-1.5BC, $Ce(NO_3)_3$ was dissolved in an ethanol solution containing a well-dispersed mixture of B_2O_3 and NCM83. After the solids were completely dissolved, the resulting solution was dried at 100 °C for 12 h and subsequently calcined at 600 °C for 5 h. XRD analysis confirmed the crystalline phase of CeO_2 by matching the diffraction peaks with the standard reference pattern (PDF #00-004-0593, Fig. S5). DFT of the CeO_2/NCM83 interface (Fig. S6) reveals a relatively low adhesion energy ($W_{ad} = -2.18$ J m^{-2}), indicating that a stable heterointerface could be readily established through strong interfacial interactions. Furthermore, STEM-EDS elemental mapping was employed to analyze the spatial distribution of constituent elements in NCM83-1.5BC particles (Fig. 2f). The EDS results clearly demonstrate homogeneous distribution of Ni and B throughout the particles with a surface enrichment of Ce. Hence, NCM83-1.5BC particles with a unique dual-modified structure of Ce-enriched surface layers and homogeneous bulk distribution of B were successfully produced by the one-step calcination process. The CeO_2 surface coating may effectively mitigate interfacial parasitic reactions between the cathode particles and organic electrolyte, and the synergistic combination of near-surface Ce doping and bulk B incorporation significantly enhances the structural integrity of NCM83-1.5BC during prolonged electrochemical cycling.

To assess the practical applicability of the B/Ce dual-modification strategy, we investigated the cycling stability of the NCM83-1.5BC cathode in a half-cell within 2.7–4.5 V. As illustrated in Fig. 3a, the pristine NCM83 cathode demonstrates an initial discharge capacity of 223.84 mAh g^{-1} with 84.1% initial coulombic efficiency (ICE). The NCM83-1.5BC cathode exhibits comparable performance (225.33 mAh g^{-1}, 87.9% ICE), with the marginal improvement in initial coulombic efficiency attributed to the synergistic stabilization effect of CeO_6 octahedra/BO_4 tetrahedra and protective coating on both bulk and surface structures. At the current density of 10C, the NCM83 cathode retains only 147.14 mAh g^{-1}, reflecting compromised Li$^+$ conduction kinetics due to reduced lattice spacing and structural instability. In striking contrast, NCM83-1.5BC maintains 167.55 mAh g^{-1}, outperforming other B/Ce-modified samples and commercial counterparts (Fig. 3b). This enhancement is mechanistically validated by GITT analysis (Fig. S7), confirming the optimal B/Ce co-doping and CeO_2 coating effects. A notably lower lithium-ion migration barrier of 0.7843 eV is observed for the NCM83-1.5BC, in contrast to the 1.6839 eV barrier associated with its layered phase counterpart. This substantial reduction in the energy barrier demonstrates that the B/Ce dual modification strategy effectively facilitates lithium-ion transport, as corroborated by the data presented in Fig. S8. Extended cycling tests at 1C, 30 °C, within 2.7–4.5 V, reveal severe capacity degradation in NCM83 (77.3% capacity retention after 200 cycles, Fig. 3c), while modified variants NCM83-1.0BC, NCM83-1.5BC, and NCM83-2.0BC shows improved retentions of 85.5%, 97.2%, and 83.7%, respectively.
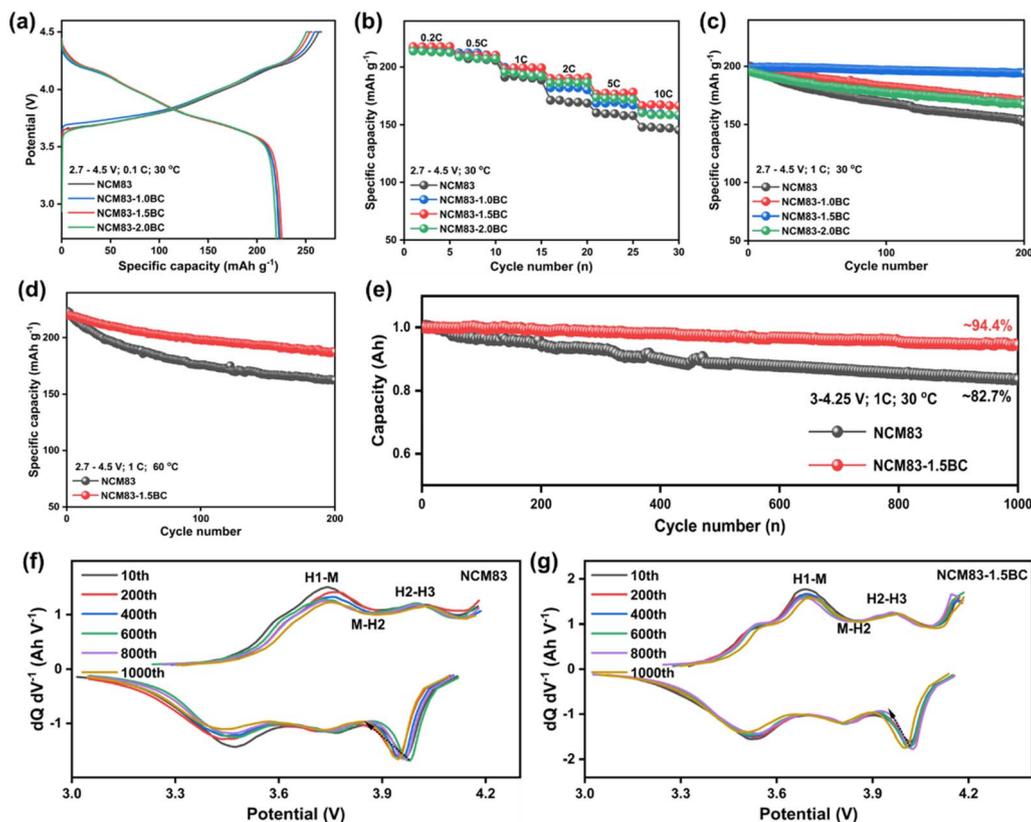
Fig. 3 (a) Initial charge–discharge curves of cathodes with various modification contents obtained at 0.1C within 2.7–4.5 V. (b) Discharge capacities of cathodes with various modification contents obtained at different currents within 2.7–4.5 V. (c and d) Cycling stability at 1C within 2.7–4.5 V for 30 °C and 60 °C. (e) The NCM83∥Gr and NCM83-1.5BC∥Gr of long-term cycling performance in pouch-type full cells at 1.0C within 3.0–4.2 V. (f and g) The dQ/dV profiles of the NCM83 and NCM-1.5BC cathode.

Elevated temperature testing (60 °C, 1C) demonstrates increased initial capacities but divergent stability profiles. NCM83 degrades to 72.8% retention after 200 cycles, whereas NCM83-1.5BC maintains 85.3% retention with 187.6 mAh g^{-1} reversible capacity after 150 cycles (Fig. 3d). Practical feasibility was further confirmed through pouch-type full-cell testing (3.0–4.2 V), where NCM83-1.5BC achieves 94.4% capacity retention after 1000 cycles at 1C, significantly surpassing NCM83 of 82.7% (Fig. 3e). Differential capacity (dQ/dV) analysis elucidates the phase transition mechanisms, revealing that while all cathodes exhibit similar phase transformation sequences, their intensity varied substantially (Fig. 3f and g). The H2 ↔ H3 transition (~4.2 V) emerges as the primary degradation source, inducing detrimental c-axis lattice contraction. Modified cathodes demonstrate effective suppression of irreversible H2 ↔ H3 transitions, confirming enhanced structural stability and electrochemical reversibility.

To investigate the operational principles of surface and bulk modifications, *in situ* X-ray diffraction analysis was performed on NCM83 and NCM83-1.5BC electrodes during the initial lithiation/delithiation process. Fig. 4a and b demonstrates that the (003) diffraction peak first moves to lower angles, reflecting c-axis elongation during the H1–H2 phase transformation due to the increased electrostatic repulsion as lithium removal. The peak shift toward higher angles is caused by the further

delithiation process, revealing abrupt c-axis compression in the H2–H3 transition, which is linked to strengthened Ni–oxygen orbital interactions and reduced lithium layer cohesion at full charge. The comparative analysis reveals significant differences in structural changes. The NCM83 sample undergoes 5.74% c-axis compression (Fig. 4c) during phase transition, markedly higher than the 3.96% observed for NCM83-1.5BC. Volume contraction (Fig. 4d) shows parallel trends, with a 7.64% reduction for NCM83 *versus* merely 5.37% for the B/Ce dual-modified NCM83. Microstructural characterizations through SEM and HRTEM provide direct evidence of strain suppression. Post-charging to 4.5 V after 100 cycles, NCM83 electrodes exhibit significant structural damage featuring grain boundary sliding (Fig. 4e). The HRTEM image reveals substantial inter-layer displacement along (003) planes, caused by TM migration and mechanical stress accumulation (Fig. 4g). Conversely, NCM83-1.5BC electrodes maintain structural integrity with minimal defects after delithiation (Fig. 4f), confirming that the synergistic effect of B/Ce co-doping and CeO$_2$ coating success-fully alleviates anisotropic strain and prevents mechanical degradation pathways (Fig. 4h).

Under conditions of elevated charge states, Ni-rich cathode materials demonstrate a pronounced tendency for oxygen loss, concurrent with permanent reduction of Ni species. This mechanism facilitates the irreversible movement of Ni^{2+} into
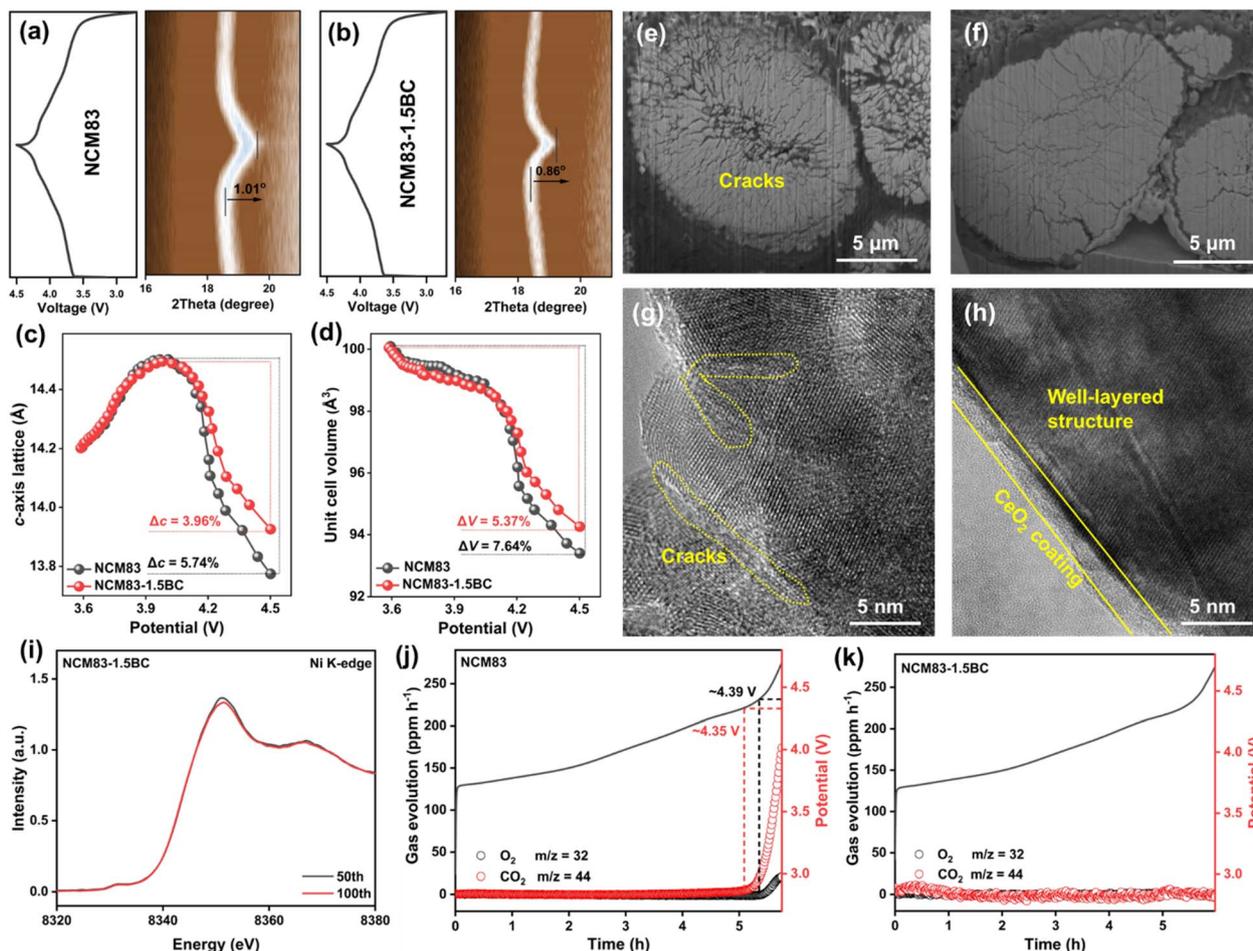
Fig. 4 *In situ* XRD of the (003) and (101) peaks for (a) NCM83 and (b) NCM83-1.5BC during the first charge cycle and corresponding changes in (c) *c*-axis parameter, and (d) unit-cell volume. SEM and HRTEM images of (e and g) NCM83 and (f and h) NCM83-1.5BC particles after charging to 4.5 V for 100 cycles. (i) Ni K-edge spectra for NCM83-1.5BC before and after 50 and 100 cycles at full charge state. (j and k) DEMS analysis of NCM83 and NCM83-1.5BC.

lithium sites, causing cation disorder and phase transition to a lithium-depleted nickel oxide structure. To investigate the changes in nickel valence states within NCM83 and NCM83-1.5BC electrodes during electrochemical processes, XANES measurements were conducted (Fig. 4i and S9). The extended cycling causes a significant decrease in Ni K-edge energy in NCM83, indicating Ni oxidation state reduction, resulting from irreversible structural changes leading to nickel oxide formation.[46,47] Conversely, NCM83-1.5BC shows minimal energy shift after long cycling, suggesting that dual B/Ce modification successfully maintains the layered framework and sustains Ni^{2+}/Ni^{4+} redox functionality. EXAFS spectral comparison in Fig. S10, after 100 cycles, the intensities of the Ni–O and Ni–TM coordination peaks for the modified material NCM83-1.5BC remain highly stable, with much less attenuation than those of the pristine NCM83. This indicates that the strong B–O bonds and the high oxygen affinity of Ce anchor oxygen atoms, preventing the formation and accumulation of oxygen vacancies during cycling and thereby stabilizing the NiO_6 octahedra. Through stabilizing the oxygen lattice and suppressing cation

mixing in the transition metal layer, the B/Ce modification significantly enhances the ordering and integrity of local structures under the harsh condition of deep delithiation, effectively mitigating oxygen loss and nickel-ion migration in the layered structure at high voltages.

To examine the B/Ce co-modification impact on gas production at high voltages, *in situ* DEMS analysis was conducted on both cathode materials. Fig. 4j and k show that O_2 and CO_2 above 4.39 V and 4.35 V are measured by only NCM83. Oxygen release corresponds to permanent lattice oxygen oxidation, while CO_2 emission typically arises from carbonate impurity breakdown (lithium residues) or electrolyte oxidation through chemical/electrochemical routes. Such oxygen loss unavoidably causes permanent structural damage. Notably, NCM83-1.5BC shows virtually no O_2 or CO_2 generation during charging, indicating exceptional lattice oxygen stability. These findings conclusively demonstrate that B/Ce co-modification adjusts $Ni^{4+}–O^{2-}$ bond covalency, effectively preventing both irreversible oxygen oxidation and electrolyte breakdown during cycling.

XPS analysis reveals that the intensities of the C 1s peak spectrum correspond to the OCO_2 (carbonate species), and other C–C and C–O bonds can be detected are lower for NCM83-1.5BC than for the pristine NCM83 (Fig. 5a). This indicates suppressed decomposition of the carbonate electrolyte on the NCM83-1.5BC cathode during cycling. Furthermore, in the F 1s and P 2p XPS spectra, the peaks corresponding to $Li_xPO_yF_z$ and TMF_x/LiF are more intense for the NCM83 sample compared to NCM83-1.5BC, suggesting more severe electrolyte decomposition (Fig. 5b and S11).[48,49] These results confirm that the CeO_2 coating layers effectively enhance the structural stability by mitigating electrolyte decomposition during cycling. To further elucidate the mechanism behind the improved cycling stability, we employed time-of-flight secondary ion mass spectrometry (TOF-SIMS) to further analyze the surface chemical composition of the cycled cathodes after 100 cycles at 1C (Fig. 5c and d). 3D reconstructions of the two cycled cathodes are presented, showing the distribution of specific fragments. The organic fragments of C_2HO^- and PO_3^- originate from the decomposition products of the carbonate solvent and $LiPF_6$ salt, respectively. LiF_2^- species originate from the decomposition of the electrolyte and the lithium plating/stripping on the active

material, which can be accelerated by the attack of acidic species such as HF.[50,51] Notably, the intensities of these fragments are lower in NCM83-1.5BC than in the pristine NCM83. According to the TOF-SIMS normalized depth profiles (Fig. 5c and d), the required sputtering time for all fragments to reach their maximum normalized intensity is shorter for NCM83-1.5BC (approximately 60 s) than for the pristine NCM83 (around 160 s). Furthermore, the detection of BO_2^- and BO^- fragments in the bulk phase signals successful boron doping into the lattice, which contributes to the enhanced structural stability of NCM83-1.5BC. The presence of a CeO_2^- surface coating effectively suppresses parasitic side reactions. These findings directly demonstrate that NCM83-1.5BC possesses a thinner cathode–electrolyte interphase (CEI) film and experiences fewer parasitic reactions on its surface.

The structural features of the cathode–electrolyte interphase (CEI) on both NCM83 and NCM83-1.5BC after 100 cycles were further investigated using cryogenic transmission electron microscopy (cryo-TEM). To prevent air exposure and preserve the structural integrity, the cycled samples were transferred to an argon-filled glove box and stored in liquid nitrogen before cryo-TEM analysis (Fig. 5e and f). Cryo-TEM analysis reveals
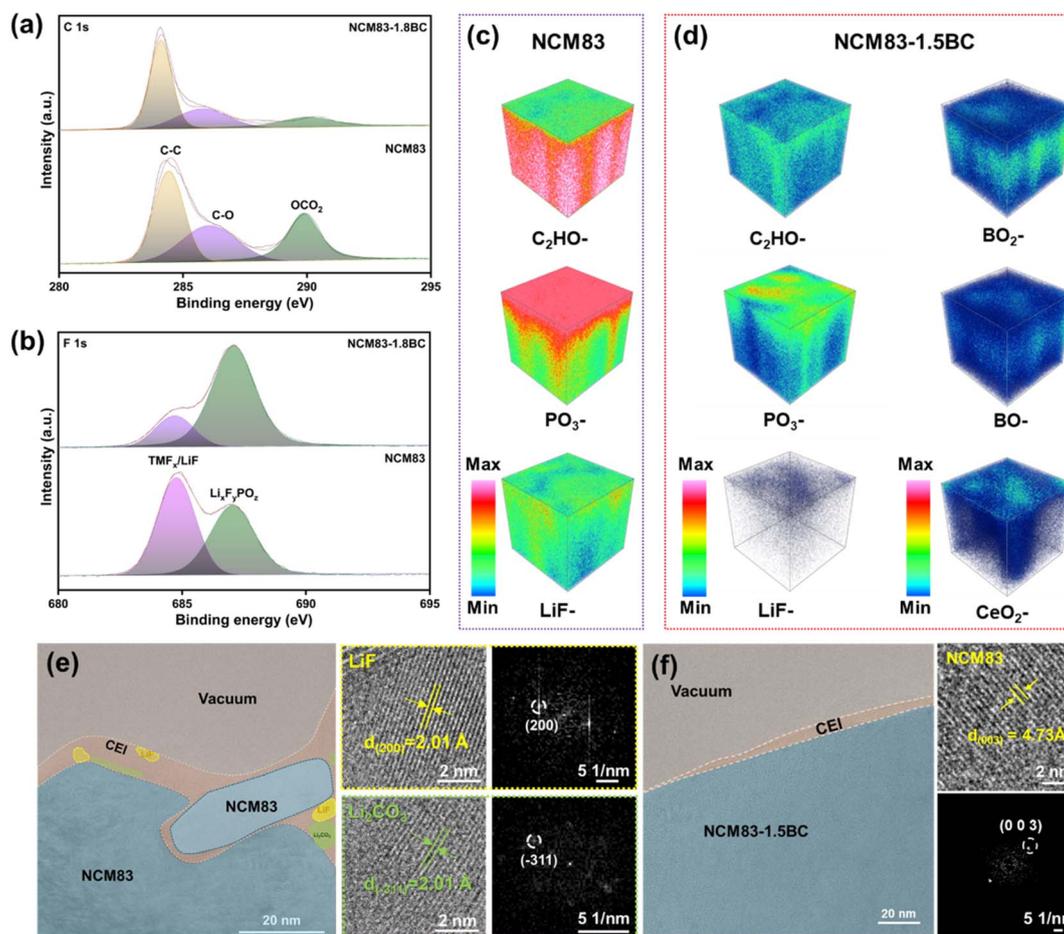

Fig. 5 XPS of (a) C 1s, (b) F 1s for NCM83 and NCM83-1.5BC after 100th cycles between 2.7 and 4.5 V. (c and d) C_2HO^-, PO_3^-, LiF^-, BO_2^-, BO^- and CeO_2^- fragments at the surface of NCM83 and NCM83-1.5BC cathodes after 100 cycles. (e and f) Cryo-EM images of NCM83 and NCM83-1.5BC cathode surface after 100 cycles.
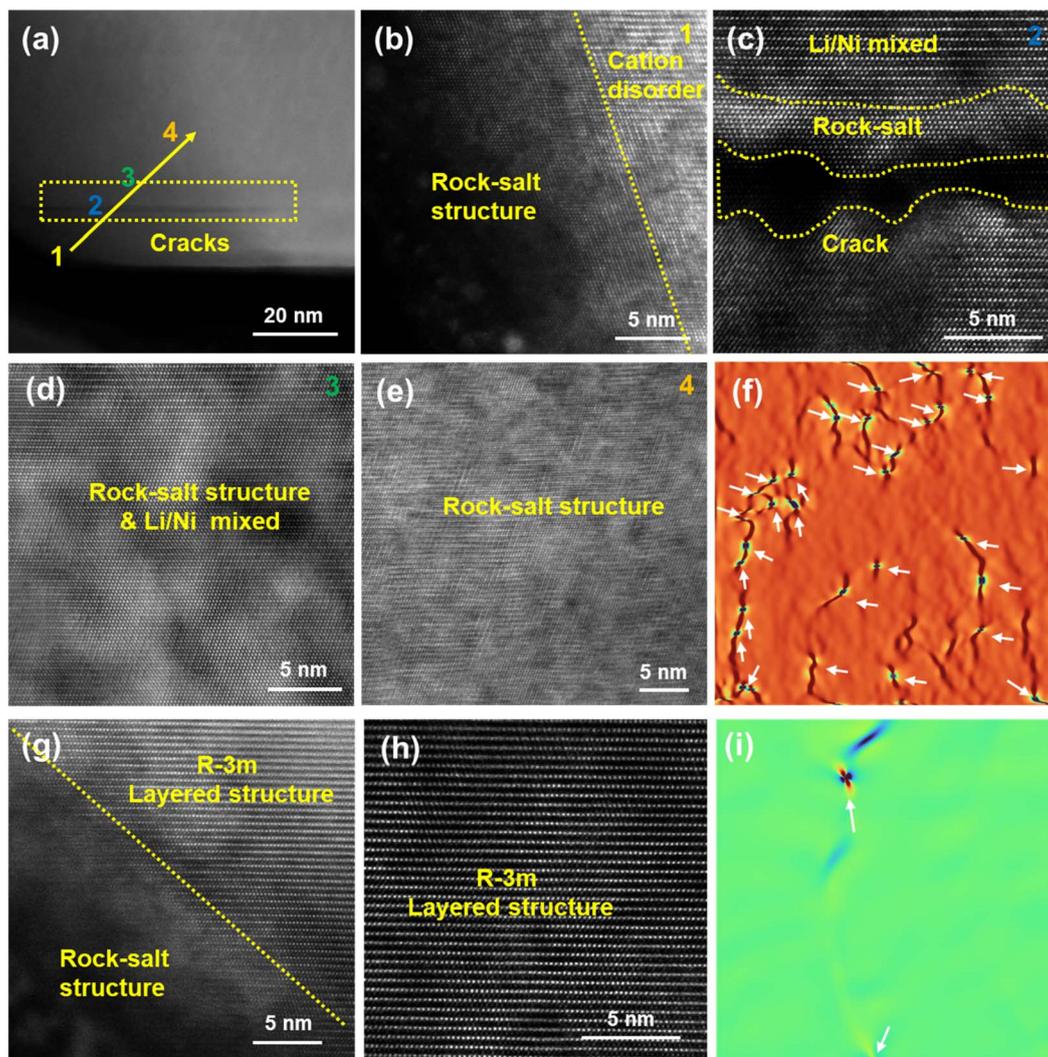
Fig. 6 Low-magnification HAADF-STEM images of (a) cross-section and (b–e) magnified HAADF-STEM images taken from the corresponding areas for NCM83 after 200 cycles at 1C, and (f) the corresponding strain state observed by GPA for (e). (g and h) HAADF-STEM images for NCM83-1.5BC after 200 cycles at 1C, and (i) the corresponding strain state observed by GPA for (h).

significant differences in the CEI morphology between the two cycled samples. The cycled NCM83 cathode exhibits a relatively thick CEI layer, extensive phase transformation in the subsurface region, and minimal retention of the internal layered structure (Fig. S12). During deep delithiation, NCM83 undergoes oxygen loss, particularly in the surface and near-surface regions, which further destabilizes the TM layer. This triggers the transformation of the layered structure into the thermodynamically more stable rock-salt or spinel phase. The H2 to H3 phase transition is accompanied by a significant contraction of the c-axis lattice, generating substantial aniso-tropic strain. This strain accumulates within the interior and interfaces of NCM83, initiating microcracks, exacerbating lattice distortion and atomic rearrangement. This process provides both the driving force and defect pathways for phase transformation in the subsurface region. The highly oxidative Ni^{4+} species on the surface accelerates electrolyte decomposi-tion and its own reduction. This reduction process is likely

accompanied by local structural reorganization, promoting the extension of the phase transformation from the surface into the subsurface region. Furthermore, phase identification indicates that the CEI primarily consists of LiF and Li_2CO_3, as evidenced by the presence of lattice fringes corresponding to the (200) and (−311) lattice planes. Notably, no crystalline LiF particles are detected, suggesting that the fluoride species within the CEI remain an amorphous state. In contrast, the cycled NCM83-1.5BC cathode possesses a thinner CEI layer and well-preserved internal layered structure, as confirmed by the observed lattice fringes of the (003) lattice plane. Combined with the TOF-SIMS results, the reduced CEI thickness further demonstrates that the B/Ce modification strategy effectively suppresses oxygen loss, enhances the stability of the lattice oxygen and the overall structure, and minimizes CEI formation.

Following the electrochemical cycling after 200 cycles within 2.7–4.5 V, a cross-sectional low-magnification HAADF-STEM image demonstrates substantial fracture development in

NCM83 cross-sections (Fig. 6a), while NCM83-1.5BC preserves its structural coherence with uniform surface characteristics (Fig. S13). Analysis of region 1 adjacent to the NCM83 surface uncovers a rock salt phase domain measuring about 5 nm in thickness, exhibiting cation disorder structure (Fig. 6b). This observation correlates with the reduced formation energy associated with surface oxygen defects and intensified interfacial side reactions. The oxygen vacancy formation energy for the NCM83-1.5BC sample is 2.092 eV, a value higher than the 1.393 eV measured for the NCM83 (Fig. S14). The increased energy requirement implies that the B/Ce co-modified material possesses a superior resistance to oxygen migration and loss from its lattice structure. Furthermore, the enhanced stability was assessed by calculating the Li^+/Ni^{2+} cation mixing energy. The energy barrier for Ni^{2+} migration into the Li layer is 1.832 eV in the modified NCM83-1.5BC, considerably greater than the 0.679 eV required in the unmodified NCM83 (Fig. S15). This elevated energy barrier effectively suppresses cation mixing, thereby inhibiting planar sliding and mitigating interlayer rupture during extended electrochemical cycling. Remarkably, the fracture boundaries are depicted in Fig. 6c, displaying the deteriorated rock salt arrangements and considerable crystalline deformations (region 2). The formation of rock salt configurations, whether occurring superficially or within the material matrix, severely undermines structural reversibility and hinders lithium-ion transport dynamics, leading to permanent structural damage and diminished electrochemical functionality. Additionally, pervasive rock salt domains and ionic disarray patterns were detected across the NCM83 (Fig. 6d and e; regions 3 and 4). Geometric phase evaluation (GPA) verifies extensive crystalline deformations in NCM83 (Fig. 6f). Conversely, the B/Ce co-modified NCM83-1.5BC sustains an impeccably organized layered architecture both superficially and internally (Fig. 6g and h), showing negligible rock salt phase formation at the surface, thereby exhibiting outstanding structural uniformity and durability. GPA confirms that only minor crystal deformation is present in NCM83-1.5BC (Fig. 6i). As a result, NCM83-1.5BC displays enhanced mechanical robustness throughout cycling, efficiently mitigating crystalline stress and deformation while maintaining structural integrity.

3. Conclusions

In summary, a novel synchronous bulk-to-surface multifunctionally full-scale modification method is developed to increase the chemical–mechanical robustness of Ni-rich layered cathodes. The cooperative effect between CeO_6 octahedral and BO_4 tetrahedral units establishes a "stabilization mechanism" that effectively reduces the lattice strain owing to H2–H3 phase changes and preserves oxygen lattice integrity, significantly suppressing cationic migration, layer slippage, and microcrack propagation during extended charge–discharge processes. Additionally, the CeO_2 surface layer improves the electrode–electrolyte interface durability and prevents detrimental surface structural transformations. As a result, the regulated NCM83-1.5BC electrode shows remarkable electrochemical durability with about 97.2% capacity retention within 2.7–4.5 V after 200

cycles at 1C, markedly outperforming the bare counterpart (77.3% capacity retention). In a practical pouch-type full cell, the cathode sustains approximately 94.4% capacity retention across 1000 cycles. This full-scale modification strategy offers substantial improvements in framework durability for Ni-rich layered oxides and presents promising prospects for next-generation high-capacity lithium-ion energy storage systems.

Author contributions

Yang Li and Zhixuan Liu conceived the idea, conducted the battery-related experiments and simulations, and prepared the draft manuscript. Zebo Gu, Junyong Deng, Guorong Liu, Kun Huang, Siyao Zhang, Hao Feng, Hao Chen, Hongxin He, and Lina Hu conducted electrochemical measurements. Fuliang Zhu participated in discussions. Haoji Wang, Jun Chen, Hongshuai Hou, and Xiaobo Ji contributed to manuscript editing, funding acquisition, and conceptualization.

Conflicts of interest

There are no conflicts to declare.

Data availability

All the data supporting this article have been included in the main text and the supplementary information (SI). Supplementary information is available. See DOI: https://doi.org/10.1039/d6sc01562j.

Acknowledgements

References

1 Y. Chu, Y. Mu, H. Gu, Y. Hu, X. Wei, L. Zou, C. Yu, X. Xu, S. Kang, K. Li, M. Han, Q. Zhang and L. Zeng, *Adv. Mater.*, 2024, **36**, 2405628.

2 Y. Chu, S. You, Y. Mu, Y. Hu, Q. Zhang, L. Zou, A. Lai, H. Wang, Q. Deng, F. Peng, Q. Zhang, H. Gu, L. Zeng and C. Yang, *ACS Nano*, 2024, **18**, 23380–23391.

3 Y. Chu, Y. Mu, L. Zou, Y. Hu, J. Cheng, B. Wu, M. Han, S. Xi, Q. Zhang and L. Zeng, *Adv. Mater.*, 2023, **35**, 2212308.

4 Y. Chu, G. Liang, Y. Mu, Q. Zhang, Y. Hu, A. Lai, H. Gu, Q. Zhang, L. Zeng and C. Yang, *ACS Nano*, 2025, **19**, 13842–13853.

5 Y. Chu, Y. Mu, L. Zou, F. Wu, L. Yang, Y. Feng and L. Zeng, *ChemElectroChem*, 2024, **11**, e202300653.

6 Y. Chu, Y. Mu, L. Zou, J. Cheng, S. Xi, Q. Pan, M. Han, H. Wang, Q. Li, F. Zheng, Q. Zhang and L. Zeng, *Chem. Eng. J.*, 2023, **465**, 142750.

7 X. Fan, X. Ou, W. Zhao, Y. Liu, B. Zhang, J. Zhang, L. Zou, L. Seidl, Y. Li, G. Hu, C. Battaglia and Y. Yang, *Nat. Commun.*, 2021, **12**, 5320.

8 S. Q. Lu, Q. Zhang, F. Meng, Y. N. Liu, J. Mao, S. Guo, M. Y. Qi, Y. S. Xu, Y. Qiao, S. D. Zhang, K. Jiang, L. Gu, Y. Xia, S. Chen, G. Chen, A. M. Cao and L. J. Wan, *J. Am. Chem. Soc.*, 2023, **145**, 7397–7407.

9 X. Qu, H. Huang, T. Wan, L. Hu, Z. Yu, Y. Liu, A. Dou, Y. Zhou, M. Su, X. Peng, H.-H. Wu, T. Wu and D. Chu, *Nano Energy*, 2022, **91**, 106665–106679.

10 L. Wang, G. Liu, R. Xu, X. Wang, L. Wang, Z. Yao, C. Zhan and J. Lu, *Adv. Energy Mater.*, 2023, **13**, 2203999.

11 L. Wang, G. Liu, R. Wang, X. Wang, L. Wang, Z. Yao, C. Zhan and J. Lu, *Adv. Mater.*, 2022, **35**, e2209483.

12 G.-L. Xu, Q. Liu, K. K. S. Lau, Y. Liu, X. Liu, H. Gao, X. Zhou, M. Zhuang, Y. Ren, J. Li, M. Shao, M. Ouyang, F. Pan, Z. Chen, K. Amine and G. Chen, *Nat. Energy*, 2019, **4**, 484–494.

13 Y. Yuan, L. Wang, Q. Sun, W. Nie, L. Chang, S. Chen and H. Cheng, *Chem. Eng. J.*, 2023, **470**, 144210.

14 K. Zou, M. Jiang, Z. Zhao, S. Xie, T. Ning, L. Tan, H. Li, Y. Zhou, W. Wang, X. Wu and L. Li, *Chem. Eng. J.*, 2023, **476**, 146793.

15 M. Cai, Y. Dong, M. Xie, W. Dong, C. Dong, P. Dai, H. Zhang, X. Wang, X. Sun, S. Zhang, M. Yoon, H. Xu, Y. Ge, J. Li and F. Huang, *Nat. Energy*, 2023, **8**, 159–168.

16 J. Cheng, B. Ouyang and K. A. Persson, *ACS Energy Lett.*, 2023, **8**, 2401–2407.

17 Y. Chu, Y. Mu, L. Zou, Y. Hu, S. Kang, H. Ren, M. Han, Q. Zhang, L. Wei and L. Zeng, *Small Struct.*, 2024, **11**, 2300247.

18 N. Y. Park, G. Cho, S. B. Kim and Y. K. Sun, *Adv. Energy Mater.*, 2023, **13**, 2204291.

19 L. Ni, H. Chen, J. Gao, Y. Mei, H. Wang, W. Deng, G. Zou, H. Hou and X. Ji, *ACS Nano*, 2023, **17**, 12759–12773.

20 L. Wang, B. Zhu, D. Xiao, X. Zhang, B. Wang, H. Li, T. Wu, S. Liu and H. Yu, *Adv. Funct. Mater.*, 2023, **33**, 2212849.

21 N. Zaker, C. Geng, D. Rathore, I. Hamam, N. Chen, P. Xiao, C. Yang, J. R. Dahn and G. A. Botton, *Adv. Funct. Mater.*, 2023, **33**, 2204291.

22 X. Zheng, R. Yu, J. Sun, Y. Chen, J. Chen, J. He, Y. Zhang, B. Han, G. Liao, J. Wu, R. Sun, C. Zhou and L. Mai, *Nano Energy*, 2023, **105**, 108000.

23 B. Jin, Z. Cui and A. Manthiram, *Angew. Chem., Int. Ed.*, 2023, **65**, 2301241.

24 J. Shen, B. Zhang, W. Huang, X. Li, Z. Xiao, J. Wang, T. Zhou, J. Wen, T. Liu, K. Amine and X. Ou, *Adv. Funct. Mater.*, 2023, **33**, 2300081.

25 T. Wang, J. Yang, H. Wang, W. Ma, M. He, Y. He and X. He, *Adv. Energy Mater.*, 2023, **13**, 2204241.

26 S. Ahmed and K. Volz, *Matter*, 2023, **6**, 1682–1684.

27 N.-Y. Park, G.-T. Park, S.-B. Kim, W. Jung, B.-C. Park and Y.-K. Sun, *ACS Energy Lett.*, 2022, **7**, 2362–2369.

28 C. Wang, X. Wang, P. Zou, R. Zhang, S. Wang, B. Song, K.-B. Low and H. L. Xin, *Matter*, 2023, **6**, 1265–1277.

29 Z. Wei, C. Liang, L. Jiang, L. Wang, S. Cheng, Q. Peng, L. Feng, W. Zhang, J. Sun and Q. Wang, *Energy Storage Mater.*, 2022, **47**, 51–60.

30 S. Sharifi-Asl, J. Lu, K. Amine and R. Shahbazian-Yassar, *Adv. Energy Mater.*, 2019, **9**, 1900551.

31 J. Chen, W. Deng, X. Gao, S. Yin, L. Yang, H. Liu, G. Zou, H. Hou and X. Ji, *ACS Nano*, 2021, **15**, 6061–6104.

32 J. Hu, L. Li, Y. Bi, J. Tao, J. Lochala, D. Liu, B. Wu, X. Cao, S. Chae, C. Wang and J. Xiao, *Energy Storage Mater.*, 2022, **47**, 195–202.

33 Z. Lu, J. Zhang, Q. Zhang, D. Wong, W. Yin, N. Zhang, Z. Chen, L. Gu, Z. Hu and X. Liu, *Adv. Sci.*, 2023, **10**, 2206442.

34 T. Zhou, X. Yu, F. Li, J. Zhang, B. Liu, L. Wang, Y. Yang, Z. Hu, J. Ma, C. Li and G. Cui, *Energy Storage Mater.*, 2023, **55**, 691–697.

35 S.-T. Myung, F. Maglia, K.-J. Park, C. S. Yoon, P. Lamp, S.-J. Kim and Y.-K. Sun, *ACS Energy Lett.*, 2016, **2**, 196–223.

36 C. Xu, A. J. Merryweather, S. S. Pandurangi, Z. Lun, D. S. Hall, V. S. Deshpande, N. A. Fleck, C. Schnedermann, A. Rao and C. P. Grey, *Joule*, 2022, **6**, 2535–2546.

37 H. Zhang, H. Liu, L. F. J. Piper, M. S. Whittingham and G. Zhou, *Chem. Rev.*, 2022, **122**, 5641–5681.

38 L. Mu, Q. Yuan, C. Tian, C. Wei, K. Zhang, J. Liu, P. Pianetta, M. M. Doeff, Y. Liu and F. Lin, *Nat. Commun.*, 2018, **9**, 2810.

39 Y. h. Luo, Q. l. Pan, H. x. Wei, Y. d. Huang, L. b. Tang, Z. y. Wang, C. Yan, J. Mao, K. h. Dai, Q. Wu, X. h. Zhang and J. c. Zheng, *Adv. Energy Mater.*, 2023, **13**, 2300125.

40 X. Tan, M. Zhang, J. Li, D. Zhang, Y. Yan and Z. Li, *Ceram. Int.*, 2020, **46**, 21888–21901.

41 Q. Gan, N. Qin, H. Yuan, L. Lu, Z. Xu and Z. Lu, *EnergyChem*, 2023, **5**, 100103.

42 C. Chen, S. Ma, M. La, L. Wei and Y. Chen, *Chem. Eng. J.*, 2025, **521**, 166926.

43 Y. J. Guo, P. F. Wang, Y. B. Niu, X. D. Zhang, Q. Li, X. Yu, M. Fan, W. P. Chen, Y. Yu, X. Liu, Q. Meng, S. Xin, Y. X. Yin and Y. G. Guo, *Nat. Commun.*, 2021, **12**, 5267–5278.

44 S. F. Amalraj, M. Talianker, B. Markovsky and D. Aurbach, *Energy Storage Mater.*, 2021, **42**, 594–607.

45 S. Kang, X. Wei, Y. Chu, Y. Mu, L. Zou, X. Xu, Q. Zhang and L. Zeng, *J. Mater. Chem. A*, 2024, **12**, 9584–9593.

46 L. Liang, M. Su, Z. Sun, L. Wang, L. Hou, H. Liu, Q. Zhang and C. Yuan, *Sci. Adv.*, 2024, **10**, 4472.

47 Q. Tong, H. Tong, C. Liang, Y. Cheng, L. Wang, Z. Yu and X. He, *Adv. Energy Mater.*, 2025, **15**, 2502841.

48 Q. Liu, Y. T. Liu, C. Zhao, Q. S. Weng, J. Deng, I. Hwang, Y. Jiang, C. Sun, T. Li, W. Xu, K. Du, A. Daali, G. L. Xu, K. Amine and G. Chen, *ACS Nano*, 2022, **16**, 14527–14538.

49 X. Cheng, X. Liu, L. Zhao, D. Zhang, J. Biao, Z. Chen, Y. Yuan, M. Liu, Y. B. He and F. Kang, *Adv. Funct. Mater.*, 2022, **33**, 2211171.

50 Z. Zhu, H. Wang, Y. Li, R. Gao, X. Xiao, Q. Yu, C. Wang, I. Waluyo, J. Ding, A. Hunt and J. Li, *Adv. Mater.*, 2020, **32**, 2005182.

51 H. Sheng, X. H. Meng, D. D. Xiao, M. Fan, W. P. Chen, J. Wan, J. Tang, Y. G. Zou, F. Wang, R. Wen, J. L. Shi and Y. G. Guo, *Adv. Mater.*, 2022, **34**, 2108947.